Journal of Materials Science: Materials in Electronics (2019) 30:21503–21513
https://doi.org/10.1007/s10854-019-02540-1

Modulation of morphology and optical characteristics of TiO_2 grown into porous silicon by an easy approach

A. Garzon-Roman[1,2] · C. Zúñiga-Islas[1] · E. Quiroga-González[2]

Received: 23 August 2019 / Accepted: 6 November 2019 / Published online: 13 November 2019
© Springer Science+Business Media, LLC, part of Springer Nature 2019

Abstract

In this work, a straightforward solvothermal approach to growing titanium dioxide (TiO_2) structures into porous silicon substrates was developed. It was possible to modulate the morphology and optical characteristics of TiO_2 by varying the concentration of the precursor and the kind of solvent. It was determined that these parameters strongly influence the morphology, photoluminescent response, bandgap, and structural characteristics of TiO_2. The morphology of the TiO_2 particles deposited on the walls of porous Si can be modulated from elongated particles to nanoflakes by increasing the precursor concentration. On the other hand, their morphology is flake-like, semi-spherical, and sea urchin-like, for methanol, ethylene glycol, and acetone, respectively. The particle size also varies with the precursor concentration; the size is smaller for lower concentrations, producing that the bandgap and emission energy increase. The variety of TiO_2 structures presented in this work, with different properties, can find potential applications in photocatalysis, solar cells, and sensing devices.

1 Introduction

Titanium dioxide (TiO_2) is one of the most important semiconductor materials. This material can be found in three crystalline phases called anatase, rutile, and brookite, with a tetragonal structure for the two first phases, while the last phase possesses an orthorhombic structure [1, 2]. Every phase can be obtained at different temperatures [3]. TiO_2 has been widely investigated due to its photoelectric properties, non-toxicity, biocompatibility, thermal stability, chemical resistance [2], and its potential application in photocatalysis [4–7], photovoltaics [8], sensors, batteries, fuel cells, and energy storage [3]. There are many ways of synthesizing TiO_2 structures, such as solgel [3], electrochemical anodization [3], sputtering [9], thermal evaporation [10], solvothermal [11], direct thermal oxidation [12], hydrothermal [13], and others [14, 15]. However, the solvothermal method has shown to be a facile and effective method to prepare TiO_2 structures in only one step, allowing to obtain different morphologies, just varying parameters such as temperature, time, additives, solution pH, and solvent medium. [16]. Photocatalysis applications have been studied for a long time; however, the efficiency of these systems is reduced due to the fast recombination of photo-generated electron–hole pairs [4]. In order to eliminate this fast recombination, TiO_2 structures have been modified with different materials. Semiconductor coupling employing immobilization of TiO_2 structures is considered to be one of the best ways to increase the photocatalytic efficiency without modifying the optical, electrical, and crystal structure of TiO_2 [4]. Catalyst supports such as carbon, carbon nanotubes, activated carbon, and porous silicon (PS) have been used [5]. Among them, one of the most promising, and underexplored supports, is PS. The immobilization of metallic oxide nanoparticles inside PS could lead to the creation of a promising technology in photocatalysis [6], because its porosity allows the interaction with atoms, ions, and molecules in applications that involve ion exchange, adsorption, and catalysis [7], and its additional (well known in electronics) semiconducting properties.

Porous silicon (PS) was discovered in 1956 [17]; however, it has been extensively studied for photonics and electronics applications just after the evidence of photoluminescence (PL) at room temperature in 1990 by Canham [18]. PS has

✉ C. Zúñiga-Islas
czuniga@inaoep.mx

✉ E. Quiroga-González
equiroga@ieee.org

[1] National Institute for Astrophysics, Optics and Electronics, Luis Enrique Erro 1, Santa Maria Tonantzintla, 72840 Puebla, Mexico

[2] Institute of Physics, Benemérita Universidad Autónoma de Puebla, PO Box J-48, 72570 Puebla, Mexico

shown intense PL, antireflective properties, and modulation of the energy bandgap [19].

Combining metallic oxides and PS results in an enhancement of the surface area and other characteristics; moreover, it modifies the electrical and optical properties of PS [20]. There are some reports about the immobilization of TiO_2 structures in PS [4–7]. However, the insertion of TiO_2 nanoparticles is commonly performed using high-cost methods such as atomic layer deposition (ALD) [4], or magnetron sputtering [21], in order to achieve uniform coatings inside the PS. In comparison with those methods, the solvothermal method can be considered a low-cost method. However, it is commonly necessary to optimize its many synthesis parameters to be able to obtain the desired crystal structures and morphologies. Nevertheless, the low effectiveness of this method is compensated by its simplicity and low cost, in comparison with ALD or sputtering. Additionally, different material morphologies can be obtained by this technique, which is not common for any other method.

In this work, the synthesis of the TiO_2 nanostructures has been carried out in one step by the low-cost and straightforward solvothermal method at low temperatures (180 °C). The solvent used and the titanium butoxide (used as the precursor) concentration have been varied to evidence how they affect the morphology, crystal structure, and morphology of TiO_2. Moreover, the PS has been synthesized by a cheap, simple, effective, and novel MACE (metal-assisted chemical etching) method. This study aims to grow TiO_2 nanostructures on and inside PS in a controlled way to observe and correlate optical, structural, and morphological properties.

2 Experimental methods

PS was prepared by MACE from Si wafers as it has been reported in [22], without illumination of the backside of the substrate. After the chemical etching, the wafers were rinsed with deionized water and dried with nitrogen.

TiO_2 was synthesized by the solvothermal method using titanium butoxide as the precursor at 180 °C. In the literature, the TiO_2 synthesis has been obtained varying the type of solvent; in this work, the precursor concentration was also varied. Hydrochloric acid (HCl) was used to add acidity to the medium (it is common to obtain nanoparticles instead of bigger particles when working in acidic medium), and ethylene glycol ($HOCH_2CH_2OH$), methanol (CH_3OH), and acetone (CH_3COCH_3) were employed as solvents. For the synthesis, two experimental setups were performed; in the first one, the titanium butoxide concentration was varied. The amount of this substance was 2, 0.25, and 0.083 mL for the experiments. It was mixed with 1 mL of HCl and dispersed into 10 mL ethylene glycol (used as solvent) in a Teflon-lined autoclave with a capacity of 15 mL under magnetic stirring for 5 min, and then a small piece of PS was introduced before closing it. Then, the autoclave was introduced into the furnace at 180 °C for 4 h. The second experimental setup was carried out varying the type of solvent. 0.083 mL of titanium butoxide and 1 mL of HCl were dispersed into 10 mL of ethylene glycol, methanol, or acetone, under the same conditions previously mentioned. After taking the autoclaves out of the oven, they were left to cool down naturally at room temperature. The samples were rinsed with deionized water and dried with nitrogen. Finally, the samples were thermally treated at 400 °C for 3 h under air. Table 1 lists the samples prepared under different conditions.

The samples were characterized by field-emission scanning electron microscopy (FE-SEM) FEI-SCIOS DualBeam in order to observe the PS morphology before and after introducing the TiO_2, in cross section and top view. Raman spectra of the samples were recorded using a Raman microscope Horiba LabRam HR, with a 632 nm laser, using a ×50 objective. Room-temperature diffuse reflectance spectroscopy of the samples was measured using a Cary 5000 UV–Vis–NIR system (Agilent Technologies Inc., Santa Clara, CA, USA). The reflectance spectra were recorded in a range from 200 to 1500 nm with a resolution of 1 nm. The photoluminescence (PL) response was measured at room temperature using a Horiba Jobin–Yvon spectrometer model FluoroMax 3 (Edison, NJ, USA) with a pulsed xenon excitation source and a multiplier tube detector controlled by a computer. The samples were excited using radiation of 330 nm, and the luminescence response was recorded in a range from 370 to 1000 nm with a resolution of 1 nm. The X-ray diffraction (XRD) diffractograms were obtained with a D8 discover Bruker diffractometer operated at 40 kV and 40 mA using the CuKα1 radiation (1.5406 Å). The TiO_2 powder diffractograms were recorded from 20° to 80° 2θ in 0.04° steps.

Table 1 Samples prepared under different conditions

Sample	Precursor solution	Proportion (V:V:V)
PTI01	Titanium butoxide/HCl/ethylene glycol (EG)	2:1:10
PTI02	Titanium butoxide/HCl/ethylene glycol (EG)	1:4:40
PTI03	Titanium butoxide/HCl/ethylene glycol (EG)	1:6:60
PTI04	Titanium butoxide/HCl/methanol (M)	1:6:60
PTI05	Titanium butoxide/HCl/acetone (A)	1:6:60

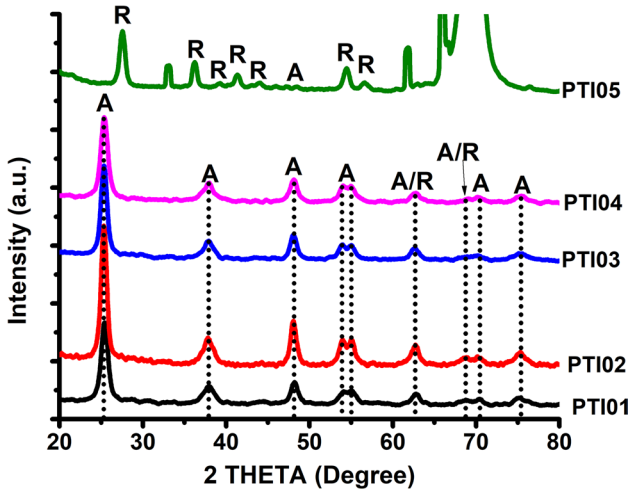

Fig. 1 XRD patterns of TiO_2 structures obtained under different processing conditions

3 Results and discussion

Figure 1 shows the XRD patterns corresponding to TiO_2 structures obtained under different processing conditions.

As can be appreciated in Fig. 1, the samples PTI01, PTI02, PTI03, and PTI04 show the characteristic peaks of TiO_2 around 25.36°, 37.88°, 48.09°, 53.99°, 55.01°, and 70.47° 2θ, associated with (101), (004), (200), (105), (211), and (220) planes, respectively. These peaks confirm that the predominant phase is the tetragonal anatase, being in good agreement with the report of [23]. However, two additional peaks found around 62.74° and 68.97° can be easily confused between the anatase and the rutile phase, due to the closed position between peaks. The peak around 62.74° can be the (204) plane of anatase or the (002) plane of rutile. The peak around 68.97° could correspond to the (116) plane of anatase or the (301) of rutile. On the other hand, sample PTI05 shows peaks distinctive of the rutile phase, around 27.51°, 36.1°, 39.13°, 41.28°, 44.01°, 54.35°, and 56.5° 2θ, which correspond to (110), (101), (200), (111), (210), (211), and (220) planes, respectively. Moreover, one additional peak around 48° can be associated with the (200) plane, which is typically related to the anatase phase. Samples tend to form monophasic TiO_2 structures (anatase or rutile). Nevertheless, some peaks are confirming the formation of mixtures with the remaining amount of a new TiO_2 polymorphic phase, as will be presented in the results of Raman.

Figure 2 shows the Raman spectra for the samples obtained under different synthesis conditions.

Raman spectroscopy was used to determine the TiO_2 phase of the samples according to the position of the peaks [1, 20, 24–28]. Figure 2 shows the Raman spectra of the different samples. Sample PTI01 shows peaks at 144 cm^{-1} [20, 25, 28], 196 cm^{-1} [24, 28], 397 cm^{-1} [25, 27, 28], 516 cm^{-1} [24, 25, 28], and 638 cm^{-1} [25, 28] which have been catalogued for anatase phase and can be assigned as the E_g, B_{1g}, A_{1g}, B_{1g} modes. Samples PTI02 and PTI03 show the peaks at 143.9 cm^{-1} [20, 25, 28], 226.9 cm^{-1} [28] 434.9 cm^{-1} [20], 620 cm^{-1} and 623 cm^{-1} [1, 20] which indicate a combination of anatase and rutile phases. Sample PTI04 shows peaks at 146 cm^{-1} (E_g) [20, 25, 28], 228.1 cm^{-1} [28], 432.1 cm^{-1} [20] and 642 cm^{-1} (B_{1g}) [25] that characterize the anatase phase. Finally, sample PTI05 shows the peaks around 144.7 cm^{-1} [20, 25, 28], 231.1 cm^{-1} (E_g) [28], 448.2 cm^{-1} (E_g) [24], and 608.8 cm^{-1} (A_{1g}) [24, 26] which correspond to the rutile phase. Mode E_g is due to the symmetric stretching vibration of O–Ti–O, the B_{1g} mode is originated from the symmetric bending vibration of O–Ti–O, and the mode A_{1g} corresponds to the antisymmetric bending vibration of O–Ti–O in TiO_2 [20].

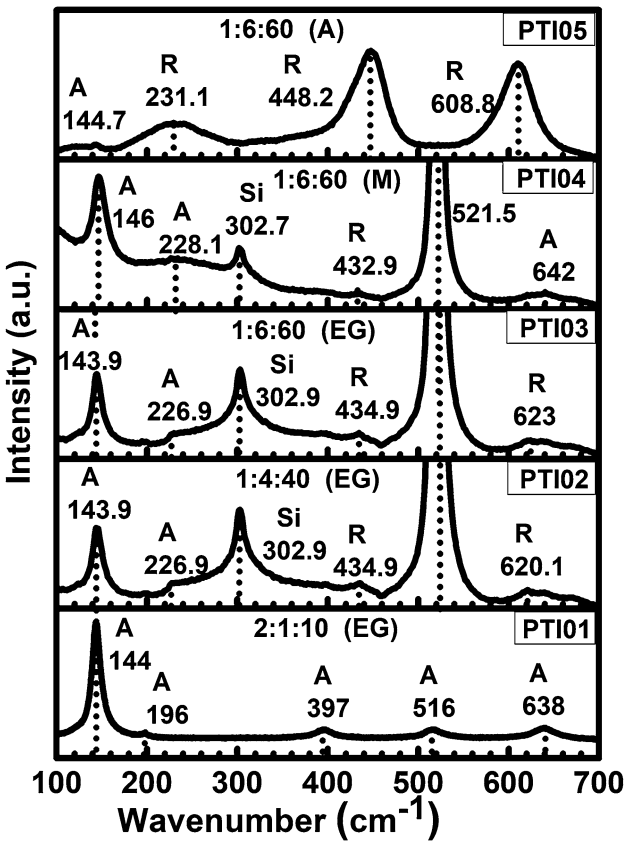

Fig. 2 Raman spectra of the PS/TiO_2 samples

On the other hand, some peaks around 302 cm^{-1} and 521 cm^{-1} are present in samples PTI02, PTI03, and PTI04; this effect is due to the lack of coating of the TiO_2 structures on the PS, as will be seen in the SEM images. According to the literature, these peaks are characteristics of crystalline silicon. Due to the formation of pores in Si, the peak at 521.5 cm^{-1} must shift to a lower frequency [20]; however, in this case, the higher-frequency shift could be explained

by any interaction effect of the TiO_2 with the PS. Also, the peak at 302 cm^{-1} is explained due to the formation of silicon nanocrystal embedded in a PS matrix [20]. Figure 3 shows the FESEM images of the top view and the cross section of PS obtained by MACE.

According to Raman, the spectra, significant differences among the samples, regarding their crystalline phase, can be observed. This is strongly related to the synthesis conditions; for example, sample PTI01 synthesized with a high titanium butoxide concentration shows the characteristic peaks for a pure anatase phase. The anatase phase could give the morphology (flake-like). Samples PTI02 and PTI03 show the same peaks almost in the same position; however, they indicate a combination of anatase and rutile phases. The combination of these phases could be related to the morphology of the TiO_2 structures; SEM images (Fig. 4) exhibit radical changes in the morphology of the samples from nanosheets (PTI01) to short nanorods (PTI02), and elongated nanoparticles (PTI03) will be observed. Sample PTI04 (methanol solvent) has almost a pure anatase phase with a peak related to the rutile phase. Meanwhile, the sample PTI05 (acetone solvent) shows almost a pure rutile phase. The combination of phases could be attributed to predominance in the agglomeration dimensionality. Reference [16] mentions that nanorods have a rutile phase, while the anatase phase is observed in nanosheets and other irregular morphologies. Also, it is important to note the predominance of the rutile phase when acetone is used. According to the literature [16], a good interface, which could separate the titanium precursor from the aqueous phase, is the key to control the formation of 3D structures, due to the control of the hydrolysis and polycondensation. The control of the morphology is the key to the predominant phase, as it was previously mentioned. Moreover, Zakrzewska [29] mentions that oxygen nonstoichiometry created at high sputtering rates promotes rutile growth. For that reason, the oxygen and the morphology

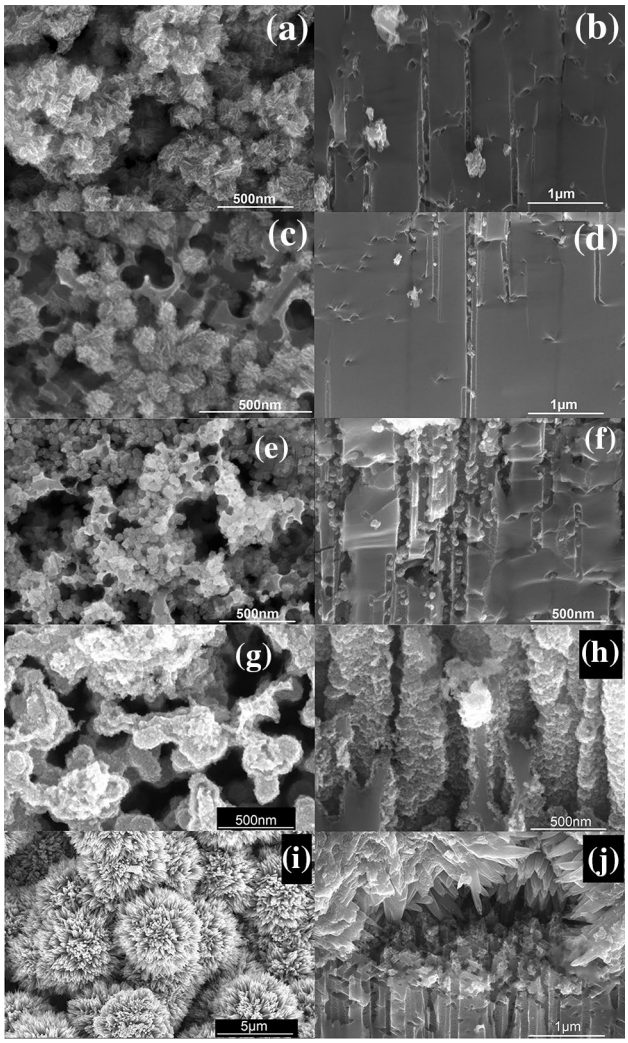

Fig. 4 SEM micrographs in top view and cross section of TiO_2 on PS **a** top-view PTI01, **b** cross section PTI01, **c** top-view PTI02, **d** cross section PTI02, **e** top-view PTI03, **f** cross section PTI03, **g** top-view PTI04, **h** cross section PTI04, **i** top-view PTI05, **j** cross section PTI05

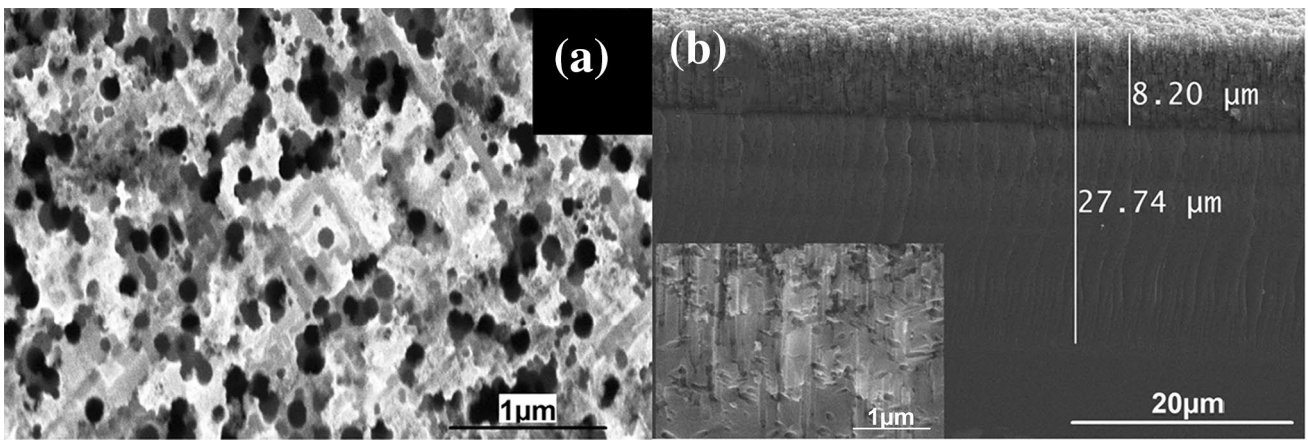

Fig. 3 SEM micrographs of the PS in **a** top view **b** cross section

could be the cause of the rutile phase formation. However, Xu et al. [16] mention that the solvent is the main promotor to generate 3D structures. The 3D structures are a result of the solvent properties such as polarity, boiling point, surface tension, dielectric constant, and more. Xu et al. [16] make an explanation for the combination of the solvent, the acid medium, and the precursor. In this explanation, the dielectric constant reflects the solvent polarity, HCl is soluble in some polar solvents, and the titanium butoxide is soluble in only organic solvents. A high concentration of H^+ and Cl^- at the interface promotes the formation of the rutile phase, and the selective adsorption of Cl^- ions on the rutile (110) plane creates the growth along [001] direction to form rutile nanorods. Therefore, Xu et al. [16] inferred that an excellent liquid–liquid interface isolates the precursor agent from the aqueous phase and concentrate HCl. Therefore, using acetone makes a good interface, which is favorable for the formation of the quasi-3D urchin-like hierarchical microsphere structures. In the resume, the phase of the TiO_2 is related to the structure (3D agglomerates due to 1D structures), and the structure is connected with liquid–liquid interface of the elements in the solution.

Figure 3 shows the FESEM images of the top view and the cross section of PS obtained by MACE.

Figure 3a shows the microstructural characteristics (top view) of PS substrate with 30 min of chemical etching, and it is possible to observe a sponge-like structure very similar to conventional electrochemical anodization. According to Fig. 3a, pores have a uniform distribution, circular morphology, and similar sizes. This microstructure correlates with the geometry of the metal particles used to generate pores in PS. The macropores formation could be related to the combined effect of the Ag nanoparticle size and the etching time. In this case, the pore size category falls into macropores, since the pore size turned out to be over 50 nm [30].

Figure 3b shows the cross section of the PS. Cross section micrograph of PS after 30 min of etching shows channels surrounded with a skeleton of crystalline silicon nanowires [18]; these structures appreciate in the inset image. Also, two regions of the PS are visible; the first region has a thickness of around 8 µm, and the second region has a thickness of around 20 µm. This phenomenon could be attributed to the nature of the chemical etching, since the maximum concentration of the Ag nanoparticles reaches a limit at a specific region, causing a reduction in the number of pores. Another explanation could be due to a non-perfectly orthogonal tilt of the samples during the imaging or defects obtained by the cleavage. The thickness of the porous silicon layers is around 28 µm for 30 min, indicating that the etching rate is close to 0.93 µm per minute.

Figure 4 shows the top view and cross section of the samples of PS/TiO_2, varying the titanium butoxide concentration and the solvent. Figure 4a and b shows TiO_2 on the PS synthesized with 2:1:10 of titanium butoxide, HCl, and ethylene glycol in volume ratio, respectively. A disordered morphology of loosely packed flocs assembled from 2D nanosheets with irregular shapes can be observed, and similar 2D structures have been reported by Xu et al. [16]. Nanosheets fully cover the PS surface, even blocking the view of silicon pores. Nevertheless, the cross section shows some pores with a partial infiltration of TiO_2 agglomerates. The TiO_2 partial infiltration can be attributed to the size of these agglomerates, which is bigger than the pore diameter; moreover, the surface tension and the viscosity of the ethylene glycol may affect capillary pressure and absorption capacity of the solution, allowing wettability conditions into the pores.

Figure 4c and d shows the TiO_2 structures synthesized with 1:4:40 of titanium butoxide, HCl, and ethylene glycol in volume ratio, respectively, in top view and cross section. Figure 4c shows that TiO_2 morphology and size change considerably compared to the first case (2:1:10) since it can be observed spheres with a regular structure and a well-defined shape. These spherical structures seem to be as TiO_2 agglomeration of short nanorods. This effect is contradictory to what is mentioned by Xu et al. [16], where they mentioned that the use of ethylene glycol constitutes the formation of irregular structures without distinct shape building blocks. Another interesting thing that observes is that these sphere structures possess a similar size to the pores, or even smaller than the pores, which makes the introduction of the spheres inside of them possible. Figure 4c shows some spheres inside of the pores. Figure 4d shows a cross section to corroborate the introduction of these spheres.

However, as can be seen, only some spheres can be appreciated; this could be because the size of the TiO_2 structures is comparable with the pore size, which generates a bottleneck along the channel. Thus, the introduction of TiO_2 particles along the Si channel is inhibited.

Figure 4e and f shows the top-view and cross section FESEM images of TiO_2 structures synthesized with 1:6:60 of titanium butoxide, HCl, and ethylene glycol in volume ratio, respectively. Figure 4e presents a new morphology concerning the previous experiments shown. In this case, the size of the agglomerates decreases considerably, and the spherical form remains unchanged as in the second case (1:4:40, Fig. 4c and d). TiO_2 nanospheres decorate the PS surface. In Fig. 4f, the cross section shows pores with nanospheres decorating along the Si channel. Hence, it is demonstrated that titanium butoxide concentration plays an important role in morphology and size control. Since, in the first case (2:1:10), the morphology turns out to be nanosheets or nanoflakes, in the second case (1:4:40) the morphology seems to be short nanorods and in the third case (1:6:60 volume ratio) the morphology drives to the agglomeration of nanoparticles.

Figure 4g and h shows the top-view and cross section FESEM images of TiO_2 structures synthesized under the following conditions: 1:6:60 of titanium butoxide, HCl, and methanol volume ratio, respectively. According to the top-view FESEM image (Fig. 4g), a radical change in comparison with the other experiments can be observed; in this case, the formation of TiO_2 regular nanoparticles (size ~ 15 nm) is evident; this morphology is slightly similar to Fig. 4e. However, size is smaller than using ethylene glycol. Likewise, it can be appreciated that nanoparticles cover the fulfill surface of the PS and the Si channels; this coating is a conformal deposit. Figure 4h shows the cross section of the sample with 1:6:60 of titanium butoxide, HCl, and methanol volume ratio. Figure 4h corroborates the coating of the Si surface and channels by TiO_2 nanoparticles like a conformal deposit. It is well known that sophisticated processing methods only reach conformal deposits such as sputtering, ALD, plasma, or PECVD [4, 21, 31, 32].

Finally, Fig. 4i and j shows the top-view and cross section images of TiO_2 structures synthesized with 1:6:60 of titanium butoxide, HCl, and acetone volume ratio, respectively. Figure 4i shows micro-flower structures composed of a large number of nanorods along the radial direction from the core to the surface. Something similar has been reported by Xu et al. [16] with similar sizes. Figure 4j shows the cross section of the PS/TiO_2 sample; however, because the size of these micro-flowers is ten times bigger than the pore size, the insertion of these TiO_2 structures was impossible.

The morphology observed in SEM images clearly shows a tendency both changing the alkoxide concentration and varying the solvent. The variation of butoxide concentration results in the morphology and size structures from bigger (agglomeration of nanosheets with the highest concentration) to smaller structures (nanospheres and nanoparticles with the lowest concentration). Moreover, the change of the solvent results in the variation of the morphology or size. The EG solvent generates irregular nanoparticles of around 50 nm, and the M solvent promotes the formation of perfect nanoparticles of approximately 15 nm. However, the A solvent creates a change in morphology and size as urchin-like micrometric structures. Therefore, the concentration of the titanium precursor and solvent variation can modify the morphology and size of the TiO_2 structures.

Regarding the coating in the PS, under certain conditions, it is possible to obtain complete coverage of the PS structure, and this is related to the morphology and size of the TiO_2 structures. SEM images show different morphologies. Therefore, correlating the results of Raman and XRD, it could be said that 3D structures tend to have a rutile phase if the structures are formed by 1D structures (nanorods); meanwhile, the anatase phase is produced by 2D agglomeration structures. Thus, the morphology of the TiO2 plays an important role in obtaining a specific phase and morphology because it depends on both alkoxide concentration and the solvent, as previously mentioned.

The SEM microscope is also equipped with energy-dispersive X-ray spectroscopy (EDX) for elemental analysis. The results show that TiO_2 structures are supported in the PS. In some cases, the TiO_2 stoichiometry can be confirmed, but in special cases (PTI05), there is an excess of Ti, due to the large microstructure of Ti. The results are summarized in Table 2.

The pore coverage was calculated, taking the cross section image of each sample. In this case, it was taken the average of the area (the Si channel was idealized as a cylinder) from different Si channels and the coating area by the TiO_2.

Photoluminescence spectra are presented in order to know the luminescent effect produced before and after depositing TiO_2 structures. Analyzing PL signals is very important in order to understand the behavior of photons generated

Table 2 Characteristics of TiO_2 prepared under different conditions: atomic percentage of composing elements (at.%), empirical formula, morphology and size, and pore wall coverage

Sample	Elements (atomic%)		Stoichiometry		
	Ti (at.%)	O (at.%)	Empirical formula	Morphology and size	Pore wall coverage % (C)
PTI01 (2:1:10) (EG)	33.89	66.1	$TiO_{1.95}$	Nanosheets agglomeration 2D (500 nm)	10
PTI02 (1:4:40) (EG)	32.05	67.94	$TiO_{2.12}$	Nanospheres with short nanorods (100 nm)	25
PTI03 (1:6:60) (EG)	37.59	62.41	$TiO_{1.66}$	Elongated nanoparticles (50 nm)	40
PTI04 (1:6:60) (M)	39.21	60.78	$TiO_{1.55}$	Nanoparticles around 15 nm	100
PTI05 (1:6:60) (A)	34.01	65.99	$TiO_{1.94}$	Microspheres with nanorods (5–6 µm)	0

by the electron–hole recombination effect. The results are summarized in Fig. 5 for PS etching chemically and coating for TiO_2 structures. The PS shows a broadband, with a maximum emission of around 648 nm or 1.9 eV with a full width at half maximum (FWHM) around 0.5 eV, similar to Leontis et al. [33]. Moreover, it is possible to observe a weak shoulder around 807 nm. In this case, the PL effect could be due to the structure and morphology of the PS, since the porosity can be seen as Si nanocrystals interconnected with different sizes along with the tubular structure [33]. The peak position of the PL depends mainly on the size distribution and chemical composition [33]. In order to explain the origin of the PL in these porous structures, many models have been proposed as quantum confinement [34, 35], hydrogen termination in nanocrystals [36], oxidized nanocrystals [35, 37], localized states [35, 37], and structural defects at the surface [33, 38]. The most accepted model is quantum confinement. This effect takes advantage when the crystalline Si size is comparable with the Bohr radius of excitons in the Si crystals (around 5 nm) [39]. A study performed by Cong et al. [39] mentions that the PL peak at 700 nm is due to the quantum confinement originated by Si nanocrystal coating silicon nanowires. Also, they have a slight emission

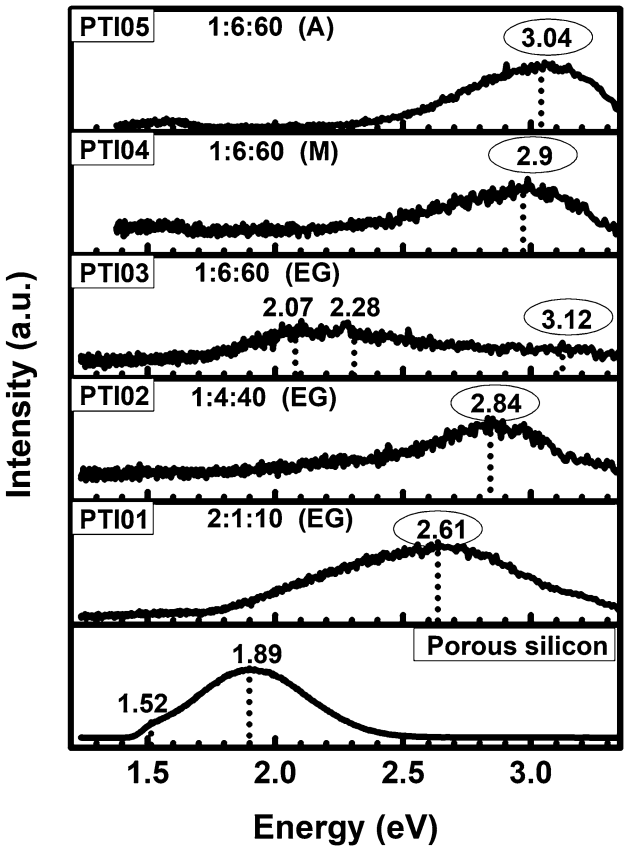

Fig. 5 PL spectra of the PS and PS/TiO_2 samples (1-column fitting image)

of around 800 nm, as in this study. This effect attributes to electron–hole recombination confined in Si crystals with a diameter of a few nanometers [39]. The origin of this peak could corroborate with the Raman spectrum peaks found around 302.5 cm^{-1}, where the peak is explained, due to the formation of silicon nanocrystal embedded in a PS matrix [29]. However, it is not possible to discard effects such as oxidized nanocrystals, hydrogen-terminated crystals, or defects at the surface, since due to the preparation method, these three effects are present. A study of FTIR could confirm the first two defects (as is presented in Refs. 34 and 40); meanwhile, defects at the surface have been confirmed by SEM images (see Fig. 3a). PL could be a contribution to both defects and quantum effects.

On the other hand, the PS with TiO_2 coating has an interesting effect, as shown in Fig. 5. A passivation effect of the PS surface is evident, since the broadband at 648 nm disappears and a new blueshifting band appears. The passivation effect of the PS can corroborate with the TiO_2 coating on the PS surface. The PL for TiO_2 has been explained with three origins: the self-trapping excitons, the oxygen vacancies, and the surface states [40, 41]. However, other studies add another origin from the band-to-band transition [41].

In the literature, the PL of the anatase TiO_2 phase divides into three regions for low energies under 2.65 eV, which is attributed to TiO_2 surface states. Medium energies from 2.7 to 2.84 eV correspond to the recombination of photoinduced electrons and holes via the oxygen vacancies with two trapped electrons. High energies over 3.01 eV near band edge emission are attributed to indirect transitions [41].

In this study, it can be observed these three regions with different intensities that depending on the sample. A green emission has been observed in structure PTI03, which is sometimes reported and is due to a transition of electrons from the donor level of the oxygen vacancies in the valence band [40]. According to the literature, the oxygen vacancies are intrinsic defects and are created to maintain the charge imbalance [41]. Moreover, they seem to be the most important source in the luminescent emission for TiO_2-denominated V_o, V_o^+, and V_o^{++} [40]. PL, both PS and TiO_2, structures have been already analyzed, and it is possible to say that TiO_2 PL signal changes depending on both the synthesis conditions and morphology.

Sample PTI01 shows a maximum of PL around 2.61 eV, due to surface states generated by the recombination of photoinduced holes [41]; these surface states can be generated by the large surface area of the nanosheets (see Fig. 4a). Sample PTI02 shows a blueshifting related to PTI01, and this could be due to the reduction in titanium butoxide concentration and the morphology change from nanosheets to short nanorods (see Fig. 4c), the maximum PL is observed around 2.84 eV due to recombination from oxygen vacancies [41]. However, sample PTI03 shows a redshift around

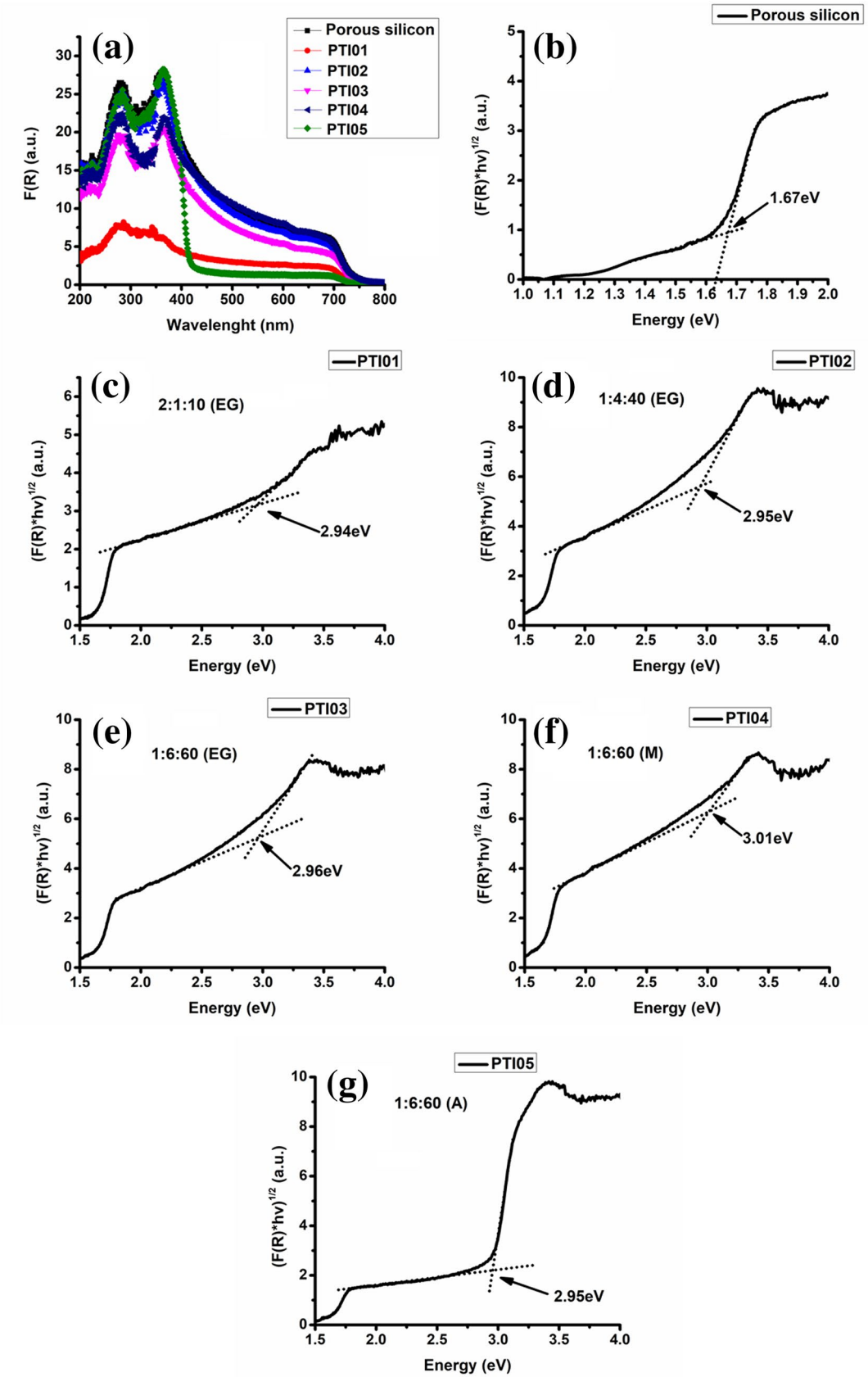
(a)
Porous silicon
PTI01
PTI02
PTI03
PTI04
PTI05
F(R) (a.u.)
Wavelenght (nm)
(b)
Porous silicon
(F(R)*hv)^1/2 (a.u.)
1.67eV
Energy (eV)
(c)
PTI01
2:1:10 (EG)
2.94eV
(d)
PTI02
1:4:40 (EG)
2.95eV
(e)
PTI03
1:6:60 (EG)
2.96eV
(f)
PTI04
1:6:60 (M)
3.01eV
(g)
PTI05
1:6:60 (A)
2.95eV

◂**Fig. 6** Diffuse reflectance of the TiO_2 structures and Kubelka–Munk method to determine the bandgap: **a** Kubelka–Munk absorption, **b** determination of E_g for PS, **c** determination of E_g for PTI01, **d** determination of E_g for PTI02, **e** determination of E_g for PTI03, **f** determination of E_g for PTI04, **g** determination of E_g for PTI05. (2-column fitting image)

2.07 and 2.28; in this case, the effect can be explained by a contribution of PS/TiO_2, since, as shown in Fig. 2e, the TiO_2 does not fully cover the PS surface; for that reason this luminescent effect can be a contribution of PS/TiO_2 interaction. Also, these peaks can be due to oxidized PS, as it is shown in Ref. [42]. This PL contribution could be present in all samples, but the PL intensity could be minimal for the rest of the samples, which avoids the observation of these contributions. However, if this contribution of the oxidized PS or the PS does not exist, the connection between alkoxide concentration and PL energy tends to grow. Also, the tendency can be related to the size of the TiO_2 structure, since as the energy increases the TiO_2 structure reduces; this is only suitable for the samples where titanium butoxide concentration reduces.

On the other hand, sample PTI05 synthesized with acetone shows the maximum PL at 3.04 eV, while sample PTI04 synthetized with methanol shows the maximum peak at 2.9 eV. Thus, the change of the solvent produced a redshift in maximum PL energy. If the highest energy for sample PTI03 is considered to be 3.12 eV, it is possible to modulate the emission energy of the TiO_2 structures, both varying the titanium butoxide concentration and changing the solvent.

Diffuse reflectance has been used in order to obtain the energy gap of the samples. By using the Kubelka–Munk method, it is possible to obtain the bandgap of the TiO_2 samples. The equation for this method is $F(R)=(1-R)^2/2R$, where R is the reflectance and $F(R)$ becomes the absorbance [43]. Since $F(R)$ represents the absorbance, in Fig. 6a, it is clear to see that there are different absorbance bands. The first absorbance band due to excited electrons from the valence band to the conduction band ranges from 250 to 300 nm, the second band runs from 350 to 400 nm, and the third band runs from 400 to 700 nm ($^2B_{1g}$ to ^2E_g transition [43]) similar to Choudhury et al. [43]. The literature reports that the valence band is composed of oxygen 2p states, and the conduction band is composed of Ti 3*d* states [43]. Spectra in Fig. 6a are similar among them; we consider that the PS contributes strongly to the absorbance spectra, which means the PS works as an active layer absorbing the UV energy. Therefore, all bands can result from the interaction between PS and TiO_2. The most important effect is present in samples PTI01 and PTI05, where the effect of TiO_2 is more evident since the contribution of the PS eliminates according to the Raman spectra (where the Si peak contribution does not appear), and the reflectance spectra corroborate with this, showing a significant difference in comparison with the other spectra. For that reason, the real nature of the TiO2 observes in these two samples because there is no interaction of the PS. Figure 6b–g shows $(F(R)*h)^{1/2}$ versus h in order to determine the bandgap of the structures. The fractional exponent is due to TiO_2, which is considered an indirect semiconductor [43]. Figure 6b shows the PS energy bandgap around 1.67 eV, similar to what reported in Ref. [44]. Bandgap for TiO_2 structures is presented in Fig. 6c–g PTI01, PTI02, PTI03, PTI05, and PTI04, which possess almost the same energy gap, 2.94 eV, 2.95 eV, 2.96 eV, 2.95 eV, and 3.01 eV, respectively. These values around 2.9 eV can be explained with Fig. 7 as a result of the insertion of the oxygen level defect close to the conduction band, which causes a direct transition from the valence band edge to the oxygen level defect [45]. This transition makes that TiO_2 structures tend to this kind of transition.

On the other hand, it is possible to observe a tendency for samples PTI01, PTI02, PTI03, and PTI04, i.e., there is an increase in the energy gap as the agglomeration size decreases. Meanwhile, sample PTI05 does not follow the tendency perhaps due to the structure obtained since, according to SEM images, it seems to be a well-defined 3D structure constituted for 1D structural arrays, in contrast with the other samples that seem to be agglomerations formed from smaller structures. Moreover, the phase change shown in the Raman spectra can be another possible option that explains the discontinuity in the tendency previously found. This effect means that sample PTI05 shows direct band-to-band transitions due to the predominant rutile phase.

Table 3 summarizes the results, where it can be appreciated the relationship between the size of the structures and the energy emission photoluminescent and the energy bandgap.

4 Conclusion

In summary, the fabrication of PS-based samples and TiO_2 using low-cost and straightforward methods has been reported. Morphologies for the PS and TiO_2 nanostructures have been reported. It was also possible to observe how the TiO_2 morphology varied not only with the solvent but also with the titanium butoxide concentration. As the precursor concentration was reduced, the morphology of the TiO_2 structure changed from 2D structures (nanosheets) to 0D structures (nanoparticles). Also, the variation of the solvent affected the morphology and the size of the TiO_2 structures from irregular nanoparticles (using ethylene glycol) to sea urchin structures (using acetone).

Moreover, under certain conditions, a conformal deposit was obtained (using methanol). Thanks to Raman spectra, it was possible to identify the different phases of TiO_2, where

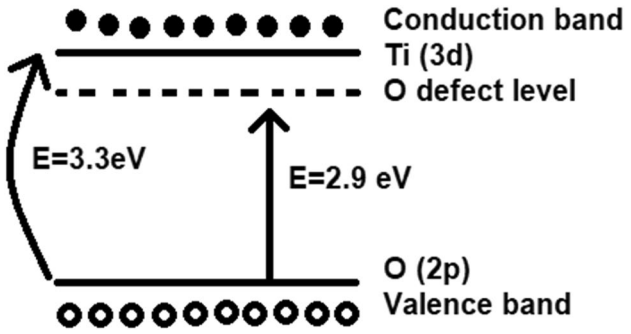

Fig. 7 Energy band diagram of TiO_2 showing the transition from the valence band to oxygen defect level. (1-column fitting image)

some samples had predominance for the anatase or the rutile phase. Also, a tendency due to the morphology can be correlated thanks to SEM analysis. This tendency means that 3D structures (PTI05) showed predominance for the rutile phase; meanwhile, 0D (nanoparticles) or 2D structures (nanosheets) displayed a tendency for the anatase phase. Something similar has been reported in the literature.

Moreover, it is possible to eliminate the Si intense peak in the samples, depending on the synthesis conditions, which cause a passivation effect on the PS surface. The XRD patterns confirmed the results obtained by Raman spectra. The patterns confirmed the predominance of any phase (anatase or rutile) for each sample related to the morphology of the TiO_2 structure. The phase combination in the samples has even been confirmed by XRD, which makes Raman spectroscopy a proper characterization technique in order to find the characteristic phases for these samples. By analyzing the PL spectra, it was possible to identify the characteristic PL band of the PS, but after depositing TiO_2, a passivation effect in the luminescence from PS was found. The PL spectra corroborated the passivation effect on the surface.

Furthermore, the TiO_2 PL can be controlled by the synthesis process, either varying solvent or modifying the titanium butoxide concentration. The reduction in the precursor concentration generated an increase in energy emission. The variation of the solvent also exhibited an energy emission modulation. On the other hand, the origin of the PL is uncertain, and it could originate from quantum confinement or structural defects on the surface of the PS; meanwhile, the luminescence of TiO_2 could be connected with oxygen vacancies or surface states. By using the Kubelka–Munk method from diffuse reflectance spectra, the energy gap of the TiO_2 samples obtained was similar to what reported in the literature. According to the energy gaps, the transitions can originate from the edge of the valence band to the oxygen level defect. By analyzing SEM images, there is even a relationship between the structure size and energy bandgap. As the size of the TiO_2 structure reduces, an increase in the energy gap finds (when the precursor concentration reduced).

This tendency is similar to the results obtained with the energy emission from PL spectra. Moreover, when the solvent was changed, the modulation of the energy gap that could be related to the TiO_2 size could also be seen. That means the acetone solvent produced the biggest structures that presented the lowest energy gap, and the methanol solvent exhibited the smallest structures that showed the biggest energy gap. In other words, SEM images have shown how the morphology variation of TiO_2 (depending on the synthesis conditions) modifies the properties of this material. The dimensionality (3D, 2D, or 0D) of the TiO_2 structure generates a phase predominance, and the size reduction in TiO_2 increases the PL emission and the energy GAP (for some cases).

Table 3 Results summarized correlating all characterization

Sample	Fesem (average size)	Pl (maximum emission peak)	Diffuse reflectance (bandgap) (eV)	Raman and XRD
PTI01 (EG)	500 nm	2.61 eV	2.94	Anatase phase
PTI02 (EG)	100 nm	2.84 eV	2.95	Combination of phases
PTI03 (EG)	50 nm	2.07 eV or 3.12 eV	2.96	Combination of phases
PTI04 (M)	15 nm	2.9 eV	3.01	Combination of phases (mainly anatase)
PTI05 (A)	5 µm	3.04 eV	2.95	Rutile phase

Acknowledgements The authors would like to thank CONACYT for its economic support through the Scholarship Number 568124.

Author contributions AGR carried out the experimental setup and the characterization and wrote the manuscript. CZI and EQG provided the idea and supervised the study. All authors read and approved the final manuscript.

Compliance with ethical standards

Conflict of interest The authors declare that they have no conflicts of interest.

References

1. S.M. Mokhtar, M.K. Ahmad, C.F. Soon, N. Nafarizal, A.B. Faridah, A.B. Suriani, M.H. Mamat, M. Shimomura, K. Murakami, Optik **154**, 510 (2018)
2. I.B. Troitskaia, T.A. Gavrilova, V.V. Atuchin, Phys. Procedia **23**, 65 (2012)
3. M. Abdullaha, S.K. Kamarudina, Renew. Sustain. Energy Rev. **76**, 212 (2017)
4. S. Sampath, P. Maydannik, T. Ivanova, M. Shestakova, T. Homola, A. Bryukvin, M. Sillanpää, R. Nagumothu, V. Alagan, Superlattices Microstruct. **97**, 155 (2016)
5. C.M. Tank, Y.S. Sakhare, N.S. Kanhe, A.B. Nawale, A.K. Das, S.V. Bhoraskar, V.L. Mathe, Solid State Sci. **13**, 1500 (2011)
6. J. Castañeda-Contreras, V.F. Marañón-Ruiz, R. Chiu-Zárate, H. Pérez-Ladrón de Guevara, R. Rodriguez, C. Michel-Uribe, Mater. Res. Bull. **47**, 290 (2012)
7. Y.S. Sakhare, S.V. Bhoraskar, V.L. Mathe, A.U. Ubale, Mater. Res. Bull. **59**, 205 (2014)
8. J. Xiong, B. Yang, J. Yuan, L. Fan, X. Hu, H. Xie, L. Lyu, R. Cui, Y. Zou, C. Zhou, D. Niu, Y. Gao, J. Yang, Org. Electron. **17**, 253 (2015)
9. D. Rafieian, W. Ogieglo, T. Savenije, R.G.H. Lammertink, AIP Adv. **5**, 97168 (2015)
10. C.W. Lai, S. Sreekantan, J. Eng. Sci. **8**, 39 (2012)
11. X.M. Yan, J. Kang, L. Gao, L. Xiong, P. Mei, Appl. Surf. Sci. **15**, 778 (2013)
12. J.M. Wu, T.W. Zhang, Y.W. Zeng, S. Hayakawa, K. Tsuru, A. Osaka, Langmuir **21**, 6995 (2005)
13. Z.Y. Yuan, B.L. Su, Colloids Surf. A **241**, 173 (2004)
14. M. Malekshahi Byranvand, A. Nemati Kharat, L. Fatholahi, Z. Malekshahi Beiranvand, J. Nanostruct. **3**, 1 (2013)
15. I. Oja, A. Mere, M. Krunks, C.-H. Solterbeck, M. Es-Souni **99–100**, 259 (2004)
16. Xu Shiping, Xiang Sun, Yuan Gao, Min Yue, Qinyan Yue, Baoyu Gao, J. Solid State Chem. **253**, 167 (2017)
17. A. Uhlir, Bell Techn. J. **35**, 333 (1956)
18. L.T. Canham, Appl. Phys. **57**, 1046 (1990)
19. Haythem Gammoudi, Fatma Belkhiria, Kamel Sahlaoui, Walid Zaghdoudi, Mahmoud Daoudi, Saloua Helali, Fabien Morote, Hassan Saadaoui, Mosbah Amlouk, Gediminas Jonusauskas, Touria Cohen-Bouhacina, Radhouane Chtouro, J. Alloy. Compd. **731**, 978 (2018)
20. P. Dwivedi, N. Chauhan, P. Vivekanandan, S. Das, D. Sakthi Kumar, S. Dhanekar, Sens. Actuators B **249**, 602 (2017)
21. Y. Wang, Y.R. Su, L. Qiao, L.X. Liu, Q. Su, C.Q. Zhu, X.Q. Liu, Nanotechnology **22**, 225702 (2011)
22. E. Quiroga-González, M.Á. Juárez-Estrada, E. Gómez-Barojas, ECS Trans. **86**, 55 (2018)
23. R. Fernández-Acosta, E. Peláez-Abellán, J.R. Correa, U. Jáuregui-Haza, Int. J. Chem. Mater. Environ. Res. **3**, 20 (2016)
24. W.F. Zhang, Y.L. He, M.S. Zhang, Z. Yin, Q. Chen, J. Phys. D **33**, 912 (2000)
25. P.M. Perillo, D.F. Rodriguez, Nanosci. Methods **1**, 194 (2012)
26. M.K. Ahmad, S.M. Mokhtar, C.F. Soon, N. Nafarizal, A.B. Suriani, A. Mohamed, M.H. Mamat, M.F. Malek, M. Shimomura, K. Murakami, J. Mater. Sci. **27**, 7920 (2016)
27. M. Najafi, A. Kermanpur, M.R. Rahimipour, A. Najafizadeh, J. Alloy. Compd. **722**, 272 (2017)
28. M. Lubas, J.J. Jasinski, M. Sitarz, L. Kurpaska, P. Podsiad, J. Jasinski, Spectrochim. Acta Part A **133**, 867 (2014)
29. K. Zakrzewska, Adv. Sci. Eng. Mater. (2011). https://doi.org/10.1155/2012/826873
30. D.H. Everett, Pure Appl. Chem. **31**, 577–638 (1972)
31. Y. Tonga, Q. Huanga, S. Ana, Q. Rena, L. Zhanga, Y. Dinga, X. Lub, Y. Zhaoa, X. Zhanga, Sol. Energy **173**, 504 (2018)
32. W.-J. Lee, Y.-H. Choa, Thin Solid Films **657**, 32 (2018)
33. I. Leontis, A. Othonos, A.G. Nassiopoulou, Nanoscale Res. Lett. **8**, 383 (2013)
34. Canham, Leigh & Knovel (Firm), London, 1997
35. Nassiopoulou A. G, Encyclopedia of Nanoscience and Nanotechnology, Silicon nanocrystals and nanowires embedded in SiO_2, ed. By Nalwa H. S. (California: American Scientific Publishers, 2004)
36. H. Mizuno, H. Koyama, N. Koshida, Appl. Phys. Lett. **8**, 3779 (1996)
37. M. Wolkin, J. Jorne, P. Fauchet, G. Allan, C. Delerue, Phys. Rev. Lett. **8**, 197 (1999)
38. E. Lioudakis, A. Othonos, A.G. Nassiopoulou, Appl. Phys. Lett. **8**, 171103 (2007)
39. L.T. Cong, N.T. Ngoc Lam, N.T. Giang, P.T. Kien, N.D. Dung, N.N. Ha, Mater. Sci. Semicond. Process. **90**, 198 (2019)
40. F. Labreche, A. Berbadj, N. Brihi, R. Karima, B. Jamoussi, Optik **172**, 63 (2018)
41. T.T. Loan, V.H. Huong, V.T. Tham, N.N. Long, Phys. B **532**, 210 (2018)
42. G. Santamaría-Juárez, E. Gómez-Barojas, E. Quiroga-González, E. Sánchez-Mora, J.A. Luna-López, Mesoporous Biomater **3**, 61 (2016)
43. B. Choudhury, M. Dey, A. Choudhury, Nano Lett. **3**, 25 (2013)
44. A. Kux, M. Ben Chorin, Phys. Rev. B **51**, 17535 (1995)
45. M.B. Sarkar, A. Mondal, B. Choudhuri, B.K. Mahajan, S. Chakrabartty, C. Ngangbam, J. Alloys Compd. **615**, 440–445 (2014)

Publisher's Note Springer Nature remains neutral with regard to jurisdictional claims in published maps and institutional affiliations.